A high-resolution study of the X-ray emission and Sunyaev–Zel'dovich effect in the Bullet cluster (1E 0657−56)

D. A. Prokhorov,[1]⋆ E. T. Million,[2]⋆ T. Akahori,[3] M. Zemcov,[4,5] A. Moraghan,[6]
S. Nagataki,[7] K. Yoshikawa,[8] S. Colafrancesco,[9,10] T. D. Rawle[11] and E. Egami[11]

[1]*W. W. Hansen Experimental Physics Laboratory, Stanford University, Stanford, CA 94305, USA*
[2]*Department of Physics and Astronomy, University of Alabama, 206 Gallalee Hall, Box 870324, Tuscaloosa, AL 35487, USA*
[3]*Korea Astronomy and Space Science Institute, Daedeokdaero 776, Yuseong, Daejeon 305-348, Korea*
[4]*Division of Physics, Mathematics & Astronomy, California Institute of Technology, Pasadena, CA 91125, USA*
[5]*Jet Propulsion Laboratory, Pasadena, CA 91109, USA*
[6]*Center for Galaxy Evolution Research and Department of Astronomy, Yonsei University, Seoul 120-749, Korea*
[7]*Yukawa Institute for Theoretical Physics, Kyoto University, Kitashirakawa Oiwake-cho, Sakyo-ku, Kyoto 606-8502, Japan*
[8]*Centre for Computational Sciences, University of Tsukuba, 1-1-1, Tennodai, Ibaraki 305-8577, Japan*
[9]*School of Physics, University of the Witwatersrand, Private Bag 3, Wits 2050, Johannesburg, South Africa*
[10]*INAF – Osservatorio Astronomico di Roma, via Frascati 33, I-00040 Monteporzio, Italy*
[11]*Steward Observatory, University of Arizona, 933 North Cherry Avenue, Tucson, AZ 85721, USA*

ABSTRACT

High-resolution imaging of the Sunyaev–Zel'dovich (SZ) effect opens new possibilities for testing the presence of various high-energy particle populations in clusters of galaxies. A detailed X-ray analysis of the 'Bullet cluster' (1E 0657−56) with *Chandra* has revealed the presence of additional X-ray spectral components beyond a simple, single-temperature plasma in its X-ray spectra. X-ray methods alone are insufficient to elucidate the origins of these spectral components. We show that the morphology and magnitude of the SZ effect at high frequencies are critically dependent upon the mechanism by which the additional X-ray spectra are created. We examine the differences between the predicted SZ effect emission maps at 600 GHz assuming the X-ray spectra are composed of thermal gas with a steep power-law index component and also thermal gas with a significant contribution of strongly heated gas. A two-temperature model with a hot ($kT \simeq 30$–40 keV) second component is the most consistent with existing SZ data at high frequencies. However, significant morphological differences remain. High-angular-resolution SZ intensity maps at high frequencies in combination with deep X-ray data provide a new window into understanding particle energization processes in the hottest, massive merging galaxy clusters.

Key words: galaxies: clusters: individual: 1E 0657 – 56.

1 INTRODUCTION

Clusters of galaxies are large structures in the Universe, with sizes of the order of Mpc. The space between galaxies in the most massive clusters is filled with a low-density ($\sim 10^{-3}$ to 10^{-2} cm^{-3}), high-temperature ($kT \sim 10$–15 keV), X-ray-emitting plasma known as the intracluster medium (ICM). The hottest galaxy cluster is 1E 0657−56, the so-called 'Bullet cluster'. The 'Bullet cluster' is an excellent example of the various effects of cluster merging on the observational properties of galaxy clusters. Of particular interest is the energy released by merger-driven shock waves, which can substantially heat the ICM. A bow shock leading the 'bullet' substructure and associated shock-heated region ($kT \sim 30$ keV) was discovered using *Chandra* (see Markevitch et al. 2002; Markevitch 2006). The very hot electron population (as well as a population of quasi-thermal electrons; see Dogiel et al. 2007) is an additional source of soft and hard X-ray emission due to bremsstrahlung. Massive merging clusters such as the 'Bullet cluster' generally also host extended, diffuse radio sources known as radio haloes (Liang et al. 2000; Ferrari et al. 2008). Because the electron synchrotron loss time is extremely short in these radio haloes, significant particle acceleration must be present. Whether this acceleration occurs at shock fronts or through merger-driven turbulence is still an area of active research (see e.g. Brunetti & Lazarian 2007). Given the evidence for significant particle acceleration from radio observations, it is

⋆E-mail: phdmitry@stanford.edu (DAP); emillion@bama.ua.edu (ETM)

reasonable to suggest that similar particle acceleration processes give rise to additional X-ray spectral components [via inverse-Compton emission from ultrarelativistic multi-GeV electrons scattered off the cosmic microwave background (CMB; see Rephaeli 1979), or via X-ray synchrotron emission of ultrarelativistic multi-TeV electrons (see Timokhin, Aharonian & Neronov 2004)]. The X-ray data obtained by the *RXTE*, *Chandra* and *Swift*/BAT missions suggest that additional X-ray spectral components are present in the 'Bullet cluster' (see Petrosian, Madejski & Luli 2006; Million & Allen 2009; Ajello et al. 2010). However, it is difficult to distinguish between the origins of these spectral components using X-ray methods alone.

The Sunyaev–Zel'dovich (SZ) effect is caused by the inverse-Compton scattering of the CMB radiation field by the hot, free electrons in galaxy clusters, changing the CMB spectrum towards massive galaxy clusters (for a review, see Birkinshaw 1999). The amplitude of the SZ effect measures the line-of-sight pressure of the electron population. Interestingly, for gas with temperatures $kT > 10$ keV, relativistic SZ corrections are significant (e.g. Rephaeli 1995) and are most important at higher frequencies. True non-thermal origins for additional X-ray spectral components (e.g. inverse-Compton emission by ultrarelativistic electrons) will have little to no effect upon the SZ effect. Therefore, the combination of X-ray and SZ methods provides a promising new avenue to disentangle the thermal and non-thermal interpretations of the detected X-ray excess in the 'Bullet cluster'. The implementation of high-angular-resolution, high-frequency SZ instruments (with angular resolution better than 1 arcmin), such as SPIRE,[1] MUSTANG[2] and LABOCA[3] (see Nord et al. 2009; Mason et al. 2010; Zemcov et al. 2010; Korngut et al. 2011) will provide important constraints upon different models of the non-thermal-like emission.[4] Recently, an SZ intensity map of the 'Bullet cluster' at a frequency of 600 GHz, with angular resolution of 36 arcsec, has been obtained with *Herschel*-SPIRE (Zemcov et al. 2010). Colafrancesco, Marchegiani & Buonanno (2011) compared the SZ intensity values at different frequencies including those of *Herschel*-SPIRE and concluded that SZ excess over that predicted from the ICM is present at high frequencies. The aim of our paper is to demonstrate how and to attempt to constrain the different particle populations residing within the 'Bullet cluster' through the useful combination of X-ray and SZ observations.

We analyse the *Chandra* data of the Bullet cluster considering various plasma models which include either an additional very hot thermal or an additional non-thermal power-law component. Using the derived plasma temperature and number density distributions from the *Chandra* X-ray data, we model the SZ intensity maps in the framework of the relativistically correct Wright formalism (Wright 1979). We demonstrate that the SZ maps are different in all our candidate models and that this fact can be used to constrain the nature of the non-thermal-like X-ray emission by means of a comparison between the modelled and observed SZ maps of the Bullet cluster.

The layout of the paper is as follows. We analyse the *Chandra* X-ray data assuming the presence of different particle populations in Section 2. We calculate the SZ intensity maps at 600 GHz in

the framework of the Wright formalism using the temperature and number density distributions obtained from the X-ray analysis in Section 3. Our discussion on how to determine the mechanism of the non-thermal-like X-ray emission from the Bullet cluster comparing the modelled and observed SZ intensity maps is presented in Section 4.1. We use 3D numerical simulations to derive the SZ intensity map of the Bullet cluster and compare it with the modelled SZ intensity map in Section 4.2. Our conclusions are presented in Section 5.

2 X-RAY ANALYSIS OF THE BULLET CLUSTER

Observations of the 'Bullet cluster' with *Chandra*, along with four other massive, merging galaxy clusters, have revealed the presence of spatially extended, non-thermal-like emission in its X-ray spectra (see Million & Allen 2009). The presence of such components has been independently confirmed using *RXTE* and *Swift*/BAT (see Petrosian et al. 2006; Ajello et al. 2010). The origins of this spectral component remain unclear. Our analysis repeats the Million & Allen (2009) analysis, making use of the updated CIAO (version 4.3) software and calibration products (CALDB version 4.4.1). Details of the analysis method can be found in Million & Allen (2009) and are quickly summarized here.

The *Chandra* observations were carried out using the Advanced CCD Imaging Spectrometer (ACIS) between 2002 July and 2004 August (see Table 1, for more details). Standard reprocessing was applied as described in Million & Allen (2009). Individual regions for spectral fitting were determined using the contour binning method of Sanders (2006), which groups neighbouring pixels of similar surface brightness until a desired signal-to-noise ratio is met. In detail, each region has ~10 000 counts. This allows us to measure the brightness of potential additional components to within 5 per cent.

The spectra were analysed using XSPEC (version 12.6; Arnaud 1996). We use the MEKAL plasma emission codes (Kaastra & Mewe 1993) and the photoelectric absorption models of Balucinska-Church & McCammon (1992). All spectral fits were carried out in the 0.6–7.0 keV energy band. The extended *C*-statistic available in XSPEC, which allows for background subtraction, was used for all fitting.

The baseline spectral model, applied to each of the 55 spatial regions, consists of an optically thin, thermal plasma model at the redshift of the cluster. We fix the Galactic absorption to 4.89×10^{20} atom cm^{-2} (determined from the Leiden/Argentine/Bonn

Table 1. Summary of *Chandra* observations. Columns list observation ID, exposure time and observation date. Each observation was taken with the ACIS-I detectors in VFAINT mode.

Obs. ID	Exp. (ks)	Obs. date
3184	82.4	2002 July 12
4984	75.9	2004 August 19
4985	24.0	2004 August 23
4986	40.7	2004 August 25
5355	22.3	2004 August 10
5356	96.2	2004 August 11
5357	78.3	2004 August 14
5358	31.7	2004 August 15
5361	82.1	2004 August 17

Radio HI survey; Kalberla et al. 2005). The temperature, metallicity and MEKAL normalization parameters[5] are free parameters for every region (in detail, the normalizations for each observation of each region are independently free). Such fits assume that the entirety of the X-ray emission is of a thermal origin. We have also performed spectral fits that assume a small portion of the X-ray emission comes from additional diffuse sources. In detail, we have performed fits in which we add a second hot thermal component or a steep power-law spectrum to the initial thermal model. For an illustration of the influence of a hot thermal component on the SZ effect, the second hot thermal component is taken to have a temperature $kT_2 = 50$ keV. We also consider other temperature values in order to generalize our results. The abundance is tied to the other temperature component and the normalization of the 50-keV hot thermal component is allowed to vary in each of the 55 regions. The steep power-law component takes the form of a power law with fixed photon index. We take $\Gamma = 1.8$ as suggested by the Ajello et al. (2010) analysis, and the power-law normalization is allowed to be free in each region. The presence of these additional components is significant at the $\sim 4\sigma$ level. We have compared the results to those of Million & Allen (2009), and the newly calibrated analysis is consistent with previous work. We also performed fits assuming different values of the second component temperature ($k_bT_e = 30$, 40 and 60 keV) and spectral index ($\Gamma = 2.0, 2.2$). We calculate the values of the MEKAL normalization parameter, K, and temperature for each individual plasma region and each thermal component in these two models of the non-thermal-like emission.

3 MODELLING SZ INTENSITY MAPS

In this section, we calculate SZ intensity maps in the framework of the two candidate models of the non-thermal-like X-ray emission from the Bullet cluster. To calculate the SZ intensity maps we use the relativistically correct Wright formalism because the plasma temperatures in the Bullet cluster are high and because it is important for the correct description of the Comptonization process of CMB photons by an additional 50-keV electron component.

3.1 Wright formalism for the SZ effect

The CMB intensity change caused by the SZ effect in the Wright formalism can be written in the form proposed by Prokhorov, Antonuccio-Delogu & Silk (2010), which is given by

$$\Delta I = I_0 \frac{\sigma_T}{m_e c^2} \int n_e k_b T_e G(x, T_e) \, dl, \qquad (1)$$

where the line-of-sight integral extends from the last scattering surface of the CMB radiation to the observer at $z = 0$, $x = h\nu/(k_b T_{CMB})$, $I_0 = 2(k_b T_e)^3/(hc)^2$, n_e is the electron number density, σ_T is the Thomson cross-section, m_e the electron mass, c the speed of light, k_b the Boltzmann constant and h the Planck constant.

The relativistic spectral function, $G(x, T_e)$, derived in the framework of the Wright formalism is written as

$$G(x, T_e) = \frac{1}{\Theta(T_e)} \int_{-\infty}^{+\infty} P_1(s, T_e) F(s, x) \, ds \qquad (2)$$

and

$$F(s, x) = \frac{x^3 \exp(-3s)}{\exp(x \exp(-s)) - 1} - \frac{x^3}{\exp(x) - 1}, \qquad (3)$$

where $\Theta = k_b T_e/m_e c^2$, s is the logarithmic frequency shift owing to a scattering (see Birkinshaw 1999) and $P_1(s, T_e)$ is the distribution of frequency shifts for a single scattering (Wright 1979; for a review, see Birkinshaw 1999). We have made a table of the spectral function values publicly available in text format on a webpage.[6] We note that this formalism is only valid in the single scattering approximation and for low values of optical depth, which is, however, sufficient for the purposes of this paper. We will apply the Wright method to calculate SZ intensity maps at a frequency of 600 GHz at which the SZ effect from the Bullet cluster has been observed by *Herschel*-SPIRE.
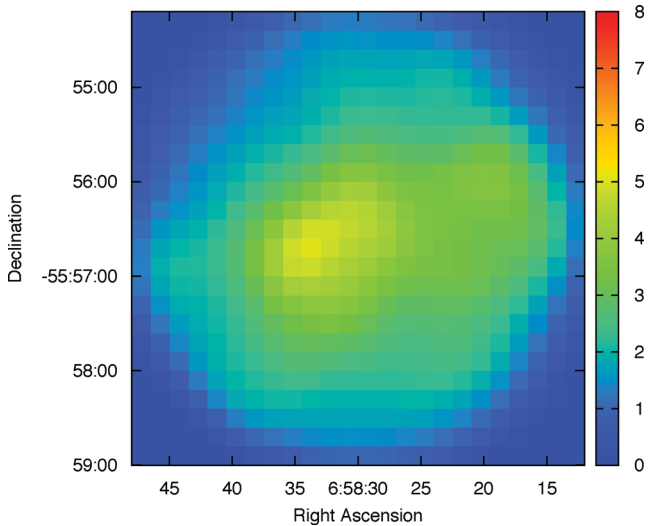
Note that an alternative method to calculate the SZ effect including SZ relativistic corrections was proposed by Challinor & Lasenby (1998) and Itoh, Kohyama & Nozawa (1998) and is based on the relativistic generalization of the Kompaneets equation, where the relativistically covariant Boltzmann collisional equation is solved. They calculated higher order relativistic SZ corrections in the form of an expansion of the CMB spectral changes into a power series of the parameter $\Theta(T_e)$. Itoh et al. (1998) also calculated the collision integral of the Boltzmann equation numerically and compared the results with those obtained by the expansion method. The convergence of the series at high frequencies, lying in the Wien region, is low at high plasma temperatures of $\simeq 50$ keV (see fig. 7 from Itoh et al. 1998). The numerical results for the relativistic corrections to the SZ effect were obtained by numerical integration of the collision term of the Boltzmann equation and were presented in the form of a table for the range of $0.002 < \Theta(T_e) < 0.100$ and $0 < x < 20$ by Itoh & Nozawa (2004). Accurate analytic fitting formulae that reproduce their numerical results for the ranges of $0.00 < \Theta(T_e) < 0.05$ and $0 < x < 20$ and of $0.05 < \Theta(T_e) < 0.10$ and $0 < x < 17$ were presented by Nozawa et al. (2000) and Itoh & Nozawa (2004), respectively. Nozawa & Kohyama (2009) demonstrated the equivalence of this formalism with the Wright formalism.

3.2 Results of modelling

To produce the SZ intensity maps at a frequency of 600 GHz we use the 2D maps of temperature and MEKAL normalization parameter obtained by using the *Chandra* data analysis in the previous section. Since the X-ray data are projected spectra, temperature and MEKAL normalization parameter information corresponds to a column of plasma through the galaxy cluster. We apply the operation of translation to produce 3D temperature and number density maps. We choose the depth along the line of sight assuming axial symmetry around the subcluster collision axis of the Bullet cluster and comparing the values of pressure integrated along the lines belonging to the perpendicular planes crossing at the collision axis. Using the Wright formalism, we calculate the SZ intensity maps and smooth the calculated SZ maps at a frequency of 600 GHz to obtain the resolution of *Herschel*-SPIRE of 36 arcsec [full width at half-maximum (FWHM)]. We choose the same pixel size as that used by Zemcov et al. (2010).

Fig. 1 shows the SZ intensity map calculated in the one-component thermal model that was presented by Million & Allen (2009). We will use this SZ intensity map for a comparison with

---

[5] The MEKAL normalization is defined as $K = \int n_e n_H dV \times 10^{-14}/(4\pi D_A^2(1 + z)^2)$, where D_A is the angular diameter distance, z is the redshift and n_e and n_H are the electron and hydrogen number densities.

[6] http://www.stanford.edu/~phdmitry/

Figure 1. The SZ intensity map of the Bullet cluster at 600 GHz derived from the one-component thermal model.

other SZ maps calculated in the models with additional electron components. All the SZ intensity maps presented in this paper are smoothed to the resolution of *Herschel*-SPIRE and are shown by the colour scale in units of mJy beam^{-1} (the beam size of *Herschel*-SPIRE at 600 GHz is used) for the sake of comparison with the SZ map observed by *Herschel*-SPIRE. The conversion from mJy beam^{-1} to MJy sr^{-1} is given by 1 mJy beam^{-1} = 0.029 MJy sr^{-1}. Note that Fig. 1 is shown by Prokhorov et al. (2011b) in their analysis of SZ map morphologies at various frequencies.

Now we produce the SZ maps using the new analysis of the *Chandra* data presented in the previous section. We plot the calculated SZ intensity map for the model including an additional non-thermal power-law component with $\Gamma = 1.8$ in Fig. 2. Note that ultrarelativistic electrons which can cause the inverse-Compton emission observed in the *Chandra* energy band are much more energetic than those having the Lorentz factor of $\gamma \simeq 3$ and contributing to the
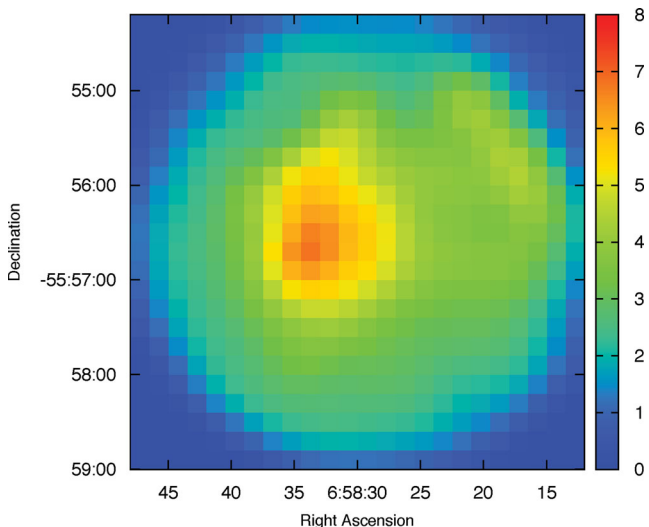
SZ effect (see Enßlin & Kaiser 2000). Therefore, we assume that ultrarelativistic electrons slightly contribute to the SZ effect. The SZ intensity map that is shown in Fig. 2 is calculated by using the 'first' thermal electron component. The morphology of this SZ intensity map is similar to that shown in Fig. 1 and, therefore, we conclude that the presence of a non-thermal power-law component in the Bullet cluster does not strongly change the SZ intensity map morphology compared to that derived from the one-component thermal model. However, the amplitude of the SZ effect is changed if the non-thermal power-law electron population emitting X-rays is present.

To produce the SZ intensity maps in the model with two thermal populations, we need to choose the values of the depth along the line of sight for both thermal components. Note that the presence of a thermal population with a very hot temperature (with $k_b T_e = 50$ keV in the previously described model) can be a consequence of heating processes which are caused by merger activity and, therefore, the depth and number density values of this very hot thermal component are model-dependent. This is because the regions of shocked plasma should be overdense compared with the ambient medium and because the heated plasma regions that are in dynamical equilibrium with the ambient medium should be sparser compared with the ambient medium. Therefore, we consider the depth of the thermal component with $k_b T_e = 50$ keV as a free parameter. As for the 'first' thermal component, we use the same procedure to determine its depth and number density as that used for the 'first' thermal component in the model including a non-thermal power-law component.

The spatial morphologies of SZ maps in the model with two thermal components depend on the ratio of their depths (note that the MEKAL parameters are fixed from the X-ray analysis) and, therefore, we can consider different possible gas distributions by assuming multiple values of the 'second' thermal component depth. The calculated SZ maps are shown in Figs 3, 4 and 5 for the different values of the depth, D_2, of a very hot thermal component that equals 10, 100 and 300 kpc, respectively. We do not consider depth values of a very hot thermal component higher than 300 kpc, because the SZ intensity that is given by the sum of the SZ intensities of the
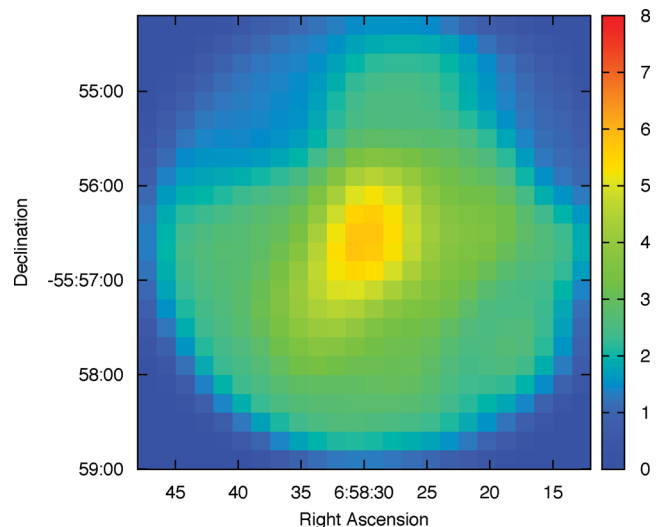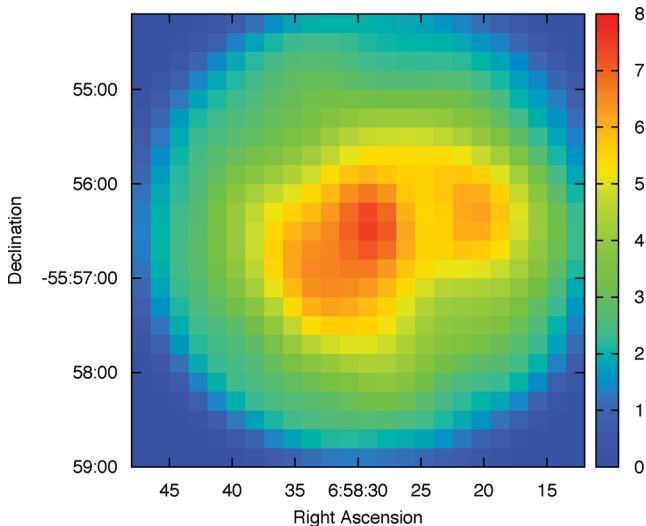

Figure 2. The SZ intensity map of the Bullet cluster at 600 GHz derived from the model including an additional non-thermal power-law component with $\Gamma = 1.8$.
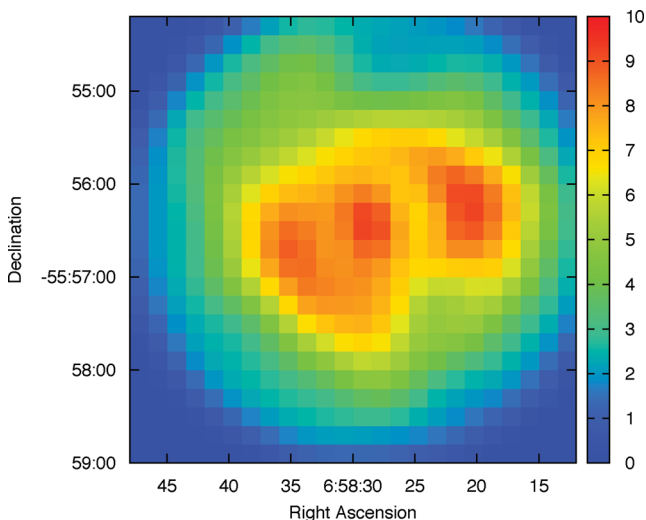

Figure 3. The SZ intensity map of the Bullet cluster at 600 GHz derived from the model with two thermal components with the depth of a very hot component of $D_2 = 10$ kpc.

Figure 4. Same as Fig. 3, except the depth of a very hot component is $D_2 = 100\,\mathrm{kpc}$.

Figure 5. Same as Fig. 3, except the depth of a very hot component is $D_2 = 300\,\mathrm{kpc}$.

two thermal components will significantly exceed the SZ intensity measured by *Herschel*-SPIRE.

Fig. 3 shows that the SZ intensity value is maximal at the centre of the SZ map that also corresponds to the centre of the MEKAL parameter and temperature maps. Since the depth of a very hot thermal component equals 10 kpc in this case, the contribution of a very hot thermal component is smaller than that in the models with a higher depth. From Fig. 3 we find that the position of the SZ intensity maximum is shifted to the west compared with that derived in the framework of the model with a non-thermal power-law population shown in Fig. 2. Therefore, the difference in the morphology of SZ intensity maps can be used to constrain particle populations residing in the Bullet cluster. Measurements of the position of the SZ intensity maximum will allow us to distinguish between the models of the X-ray excess including either a non-thermal power law or a very hot thermal electron population.

We find that the bright regions of the SZ intensity maps shown in Figs 4 and 5 are more extended than those shown in Fig. 3. The SZ intensity values are also higher on the maps shown in Figs 4 and

5 than those on the map shown in Fig. 3. This is explained by the contribution of a very hot thermal component to the SZ intensity. Note that the X-ray surface brightness is proportional to the depth, D_2, and squared number density, n_e^2, and that the SZ intensity is proportional to the depth and number density. Therefore, the SZ intensity is proportional to the square root of the depth, D_2, if the X-ray surface brightness is fixed.

The SZ intensity maps derived for other values of temperature (30, 40 and 60 keV) or power-law index (1.8 and 2.2) of the second electron component can be viewed on the webpage.[6] Comparing the SZ intensity maps obtained from the different models demonstrates that the SZ morphologies are different between hot thermal and non-thermal power-law models (see Section 4.1).

In this section, we showed that the SZ intensity maps obtained from the different models of the X-ray non-thermal-like excess are significantly different in morphology and in numerical values. This result can be used for testing different interpretations of the X-ray excess from the Bullet cluster by means of high-angular-resolution SZ observations.

4 DISCUSSION

Now we discuss the SZ observations of the Bullet cluster with the high-angular-resolution SZ instruments, *Herschel*-SPIRE (see Zemcov et al. 2010) and the Australia Telescope Compact Array (ATCA; see Malu et al. 2010), and compare the observed and modelled SZ intensity maps. We also study the possible influence of the morphological SZ effect (see Prokhorov et al. 2011b) on the position of the maximum of the absolute SZ intensity at different frequencies. In addition we present numerical simulations which allow us to demonstrate that the simulated SZ intensity map is consistent with the SZ intensity map derived in the model including an additional hot thermal component and differs from that derived in the one-component thermal model.

4.1 Observed SZ maps

In Section 3, we showed that the SZ map morphology depends on the presence of additional electron populations and that the SZ intensity map can be significantly different from that derived in the one-component thermal model. Therefore, this effect provides us with the possibility to test different interpretations of the X-ray excess from the Bullet cluster. The high-angular-resolution observations of the Bullet cluster with ATCA at a low frequency of $\simeq 19\,\mathrm{GHz}$ with FWHM of $\simeq 15$ arcsec revealed that the maximum absolute intensity value on the SZ map is at (J2000 epoch coordinates) right ascension (RA) $= 6^h58^m32\overset{s}{.}3$ and declination (Dec.) $= -55°57'03''$ (Malu et al. 2010). The position of the absolute SZ intensity maximum found by Malu et al. (2010) does not coincide with the position of the most intense X-ray emission from the eastern subcluster at RA $= 6^h58^m30^s$ and Dec. $= -55°56'28''$. The *Herschel*-SPIRE instrument provides us with new high-angular-resolution observations of the SZ effect. The SZ intensity map of the Bullet cluster has been obtained by the *Herschel*-SPIRE instrument (Zemcov et al. 2010) at a frequency of 600 GHz with angular resolution of 36 arcsec. The high-angular-resolution of *Herschel*-SPIRE and the careful subtraction of point sources performed by Zemcov et al. (2010) make *Herschel*-SPIRE the suitable instrument for studying the SZ map morphology of the Bullet cluster. In this paper, we use the results of SZ observations with *Herschel*-SPIRE to compare them with the SZ maps modelled by using X-ray observations.

To compare the observed and modelled SZ maps of the Bullet cluster we calculate the position of the SZ intensity maximum for each of the modelled SZ maps. We find that the SZ intensity peaks lie at different positions along the collision axis (that is extending along the RA axis) for different models of the non-thermal-like emission (see Figs 1–5) and, therefore, we give below the RA values for the positions of maximal SZ intensity values. The position of the SZ intensity maximum is at RA of $\simeq 6^{\rm h}58^{\rm m}34\overset{s}{.}9$ and $\simeq 6^{\rm h}58^{\rm m}34\overset{s}{.}3$ for the one-component thermal model and for the model with an additional non-thermal power-law component, respectively. The position of the SZ intensity maximum is at RA of $\simeq 6^{\rm h}58^{\rm m}31\overset{s}{.}4$, $\simeq 6^{\rm h}58^{\rm m}29\overset{s}{.}7$ and $\simeq 6^{\rm h}58^{\rm m}29\overset{s}{.}8$ for the model including two thermal components with the 'second' thermal 50-keV component depth values D_2 of 10, 100 and 300 kpc, respectively. The projected angular distance, ΔRA, between the positions of the SZ intensity maximum derived in the models with a non-thermal power-law component and with a very hot thermal component is $\simeq 0.6$ arcmin and can be probed by SZ instruments with a high angular resolution. The position of the SZ intensity maximum observed by *Herschel*-SPIRE, which is derived by calculating the centroid and uncertainty of the SZ peak in the submm source removed map, is at RA of $6^{\rm h}58^{\rm m}29\overset{s}{.}9 \pm 0\overset{s}{.}9$. This observed position of the SZ intensity maximum is more consistent in the models with an additional very hot thermal component than with the one-component thermal model and the model including an additional non-thermal power-law component. Note that the position of the SZ intensity maximum observed by *Herschel*-SPIRE is close to that of the most intense X-ray emission from the eastern subcluster.

We calculate Pearson's correlation coefficient between the observed and modelled SZ intensity values along the line that is parallel to the collision axis and is passing through the position of the SZ intensity maxima. The calculated Pearson's correlation coefficient equals 0.69 for the SZ intensity map observed by *Herschel*-SPIRE and the SZ intensity map derived in the one-component thermal model; 0.75 for the SZ intensity map observed by *Herschel*-SPIRE and the SZ intensity map derived in the model including a non-thermal power-law component; 0.88 for the SZ intensity map observed by *Herschel*-SPIRE and the SZ intensity map derived in the model including a very hot thermal component with $D_2 = 10$ kpc; 0.67 for the SZ intensity map observed by *Herschel*-SPIRE and the SZ intensity map derived in the model including a very hot thermal component with $D_2 = 100$ kpc; and 0.52 for the SZ intensity map observed by *Herschel*-SPIRE and the SZ intensity map derived in the model including a very hot thermal component with $D_2 = 300$ kpc. The squared correlation coefficient is a measure of how much of the variability in observed SZ amplitude values with RA can be 'explained by' variation in the modelled SZ amplitude values. We conclude that the model including a very hot thermal component with a small 'second' hot thermal component depth is most consistent with the *Herschel*-SPIRE observations of the Bullet cluster because the squared Pearson's correlation coefficient is closer to 1 in this case.

We present the results of a comparison between modelled and observed SZ intensity maps in Table 2. The projected angular distance, ΔRA, between the positions of the SZ intensity maxima derived from the candidate models and observed by *Herschel*-SPIRE as well as the values for Pearson's correlation coefficients are listed in this table. Pearson's correlation coefficients are largest for the model including a very hot thermal component with a small 'second' hot thermal component depth and, therefore, the SZ intensity maps derived from this model are more consistent with that observed by *Herschel*-SPIRE. The values of Pearson's correlation coefficients

Table 2. SZ effect morphologies. Columns list model, D_2, ΔRA, Pearson's correlation coefficient (PCC) and TSD along the line of sight.

Model	D_2 (kpc)	ΔRA (arcsec)	PCC	TSD (keV)
One-component	–	37	0.69 (0.87)	–
$kT_2 = 30$ keV	10	12	0.91 (0.94)	5.3
$kT_2 = 30$ keV	100	10	0.81 (0.90)	8.0
$kT_2 = 30$ keV	300	2	0.64 (0.85)	9.2
$kT_2 = 40$ keV	10	12	0.90 (0.93)	7.7
$kT_2 = 40$ keV	100	−1	0.71 (0.88)	11.8
$kT_2 = 40$ keV	300	−2	0.57 (0.83)	13.6
$kT_2 = 50$ keV	10	11	0.89 (0.92)	9.8
$kT_2 = 50$ keV	100	−2	0.67 (0.87)	15.3
$kT_2 = 50$ keV	300	−2	0.52 (0.83)	17.8
$kT_2 = 60$ keV	10	10	0.87 (0.91)	12.5
$kT_2 = 60$ keV	100	−2	0.62 (0.85)	19.4
$kT_2 = 60$ keV	300	−53	0.63 (0.81)	22.4
$\Gamma = 1.8$	–	32	0.75 (0.86)	–
$\Gamma = 2.0$	–	32	0.75 (0.86)	–
$\Gamma = 2.2$	–	32	0.75 (0.87)	–

calculated by taking all the pixels of the observed SZ map into account are listed in Table 2 in brackets and are also largest for the model including a very hot thermal component with a small 'second' hot thermal component depth.

The possible difference in the SZ map morphologies observed by ATCA and *Herschel*-SPIRE at frequencies of 19 and 600 GHz, respectively, could be caused by the morphological SZ effect (Prokhorov et al. 2011b). We derive the spectral function of $G(x, T_e)$ at a frequency of 19 GHz and calculate the SZ intensity map at 19 GHz using the gas temperature and number density maps (which are obtained from the X-ray data analysis) in the framework of the Wright formalism. The derived positions of the maximum absolute intensity value on the SZ map at 19 GHz are at RA of $\simeq 6^{\rm h}58^{\rm m}34\overset{s}{.}7$ and $\simeq 6^{\rm h}58^{\rm m}34\overset{s}{.}3$ for the one-component thermal model and for the model with an additional non-thermal power-law component, respectively. In the model with an additional very hot thermal component, we find that the maximum absolute intensity value on the SZ map at 19 GHz is at RA of $\simeq 6^{\rm h}58^{\rm m}31\overset{s}{.}4$, $\simeq 6^{\rm h}58^{\rm m}29\overset{s}{.}7$ and $\simeq 6^{\rm h}58^{\rm m}29\overset{s}{.}8$ for the 'second' thermal component depth values D_2 of 10, 100 and 300 kpc, respectively. Comparing the positions derived at frequencies of 19 and 600 GHz, we find that there is no significant morphological SZ effect and that the effect that is caused by the presence of an additional non-thermal or very hot thermal component is much stronger than the morphological SZ effect. Thus, the presence of an additional electron component can be tested by studying the morphology of SZ effect maps at each of these frequencies. Studying the reason behind why the positions of maximal SZ intensity values measured with *Herschel*-SPIRE and ATCA are different is beyond the scope of this paper.

We also calculate the central temperature standard deviation (TSD) along the line of sight in the candidate models using the temperature and depth values for the 'first' and 'second' thermal components. The TSD is given by

$$\sigma = \sqrt{\langle (k_{\rm b} T_{\rm e})^2 \rangle - \langle k_{\rm b} T_{\rm e} \rangle^2}, \tag{4}$$

where $\langle X \rangle = \int n_{\rm e} X \, {\rm d}l / \int n_{\rm e} \, {\rm d}l$, and is a measure of the inhomogeneity of the gas temperature along the line of sight. The derived values of the central TSDs are listed in Table 2 and strongly increase with temperature of the very hot electron component. Multifrequency SZ observations provide us with a method to measure the TSD along the

line of sight (Prokhorov et al. 2011a) and, therefore, provide a test of the interpretations of the non-thermal-like X-ray emission. The TSD values in the model including the 'second' thermal component with $k_b T_e = 30$–40 keV (see Table 2) are close to (10.6 ± 3.8) keV that were found from the multifrequency analysis of SZ observations of the Bullet cluster (see Prokhorov & Colafrancesco 2012). Therefore, the two-temperature model of the non-thermal-like X-ray emission from the Bullet cluster allows us to explain the observed high value of TSD along the line of sight.

We conclude that a two-temperature model with a hot second component is most consistent with the existing X-ray and SZ observations.

4.2 Simulated SZ maps

In the previous section, comparing the SZ intensity map predicted from the X-ray data analysis in the framework of the one-component thermal model with that observed by *Herschel*-SPIRE, we show that there is an offset of $\simeq 0.6$ arcmin between the positions of the SZ intensity maximum. Numerical simulations are a powerful tool for the study of X-ray and SZ intensity maps of merging galaxy clusters. We use the 3D numerical simulations presented by Akahori & Yoshikawa (2012) to study the SZ intensity map of the Bullet cluster (see also Yamada et al. 2012) and to show that the inclusion of an additional higher temperature component in the initial one-component thermal model permits us to reconcile the results of the present numerical simulations with the X-ray and SZ observations.

Akahori & Yoshikawa (2012) carried out a set of N-body and smoothed particle hydrodynamics (SPH) simulations of the Bullet cluster and increased the numbers of SPH and dark matter particles 5–10 times compared with the simulations of Springel & Farrar (2007) and Mastropietro & Burkert (2008). They consider a collision of two spherically symmetric galaxy clusters with the virial mass values of $M_1 = 1.5 \times 10^{15}$ M$_\odot$ and $M_2 = 2.5 \times 10^{14}$ M$_\odot$. The Navarro–Frenk–White density profile (Navarro, Frenk & White 1997) and β-model density profile are used for a dark matter halo and an ICM component, respectively. Initially, two galaxy clusters contact each other at their outer edge that is determined by their virial radii, and their initial relative velocity is set to 3000 km s^{-1}. The main cluster is composed of 10^7 dark matter particles and the same number of SPH particles, while the subcluster is composed of 1.7×10^6 particles of each type. The corresponding spatial resolution of SPH is 12 kpc at the ICM density of 10^{-2} cm^{-3} and 26 kpc at 10^{-3} cm^{-3}. Detailed descriptions of the code used by Akahori & Yoshikawa (2012) were published in Akahori & Yoshikawa (2010). We use the result of the simulations of the Bullet cluster system after 1.12 Gyr has elapsed from the initial conditions. At this epoch, the 'bullet' subcluster has passed the centre of the main cluster and the separation between the centres of the main cluster and subcluster equals 720 kpc, which is consistent with that observed in the Bullet cluster. The temperature map obtained in the simulations shows that a very hot plasma heated from ~8 keV to more than 30 keV by a shock wave exists to the west from the 'bullet' subcluster. This high-temperature region corresponds to the post-shock region. Another very high temperature region revealed in the simulations is located to the east from the 'bullet' subcluster and is heated by the compressive flows (see also Springel & Farrar 2007).

Using the temperature and number density 3D maps obtained from the numerical simulations of Akahori & Yoshikawa (2012), we calculated the SZ intensity map using the Wright formalism in the approach described in Prokhorov et al. (2010) and also calculated the map of squared electron number density integrated along
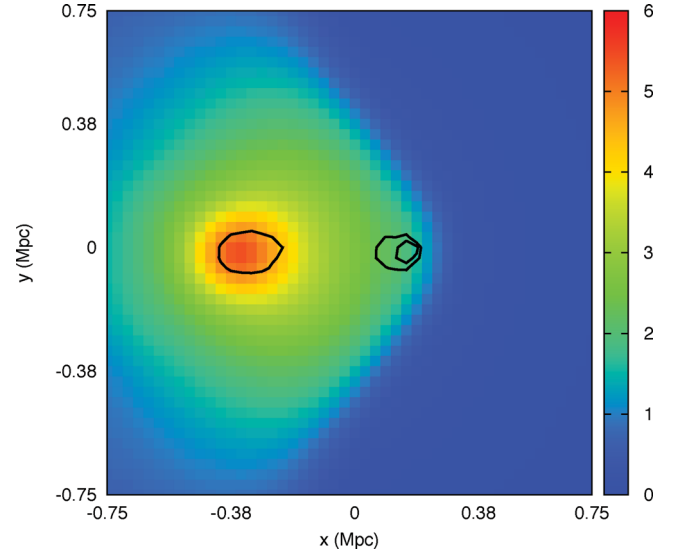

Figure 6. The SZ intensity map at a frequency of 600 GHz and the integrated squared number density map derived from the simulated maps shown by the colour scale and contours, respectively.
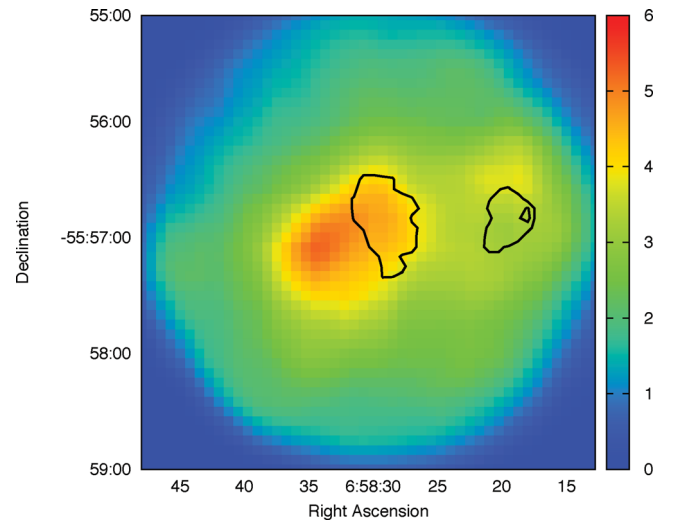
Figure 7. The modelled SZ intensity map at 600 GHz (same as in Fig. 1) and the integrated squared electron number density map, derived by assuming the one-component electron model.

the line of sight, $\int n_e^2 \, \mathrm{d}l$. Note that the X-ray surface brightness of a plasma is proportional to integrated squared electron number density and that the regions of high integrated squared number density are bright in X-rays. The SZ intensity map at a frequency of 600 GHz and the map of integrated squared electron number density derived from the simulated maps are shown in Fig. 6 by the colour scale and contours, respectively. (The simulated map shown in Fig. 6 has the same size as those shown below, but it is not centred on the eastern subcluster.) We plot the modelled SZ intensity and integrated squared electron number density maps, derived from X-ray observations by *Chandra* by assuming the one-component electron model, in Fig. 7. A comparison of Figs 6 and 7 suggests that the offset between the SZ and integrated squared electron number density for the eastern substructure is only present on the modelled map derived from X-ray observations. This difference could be explained by the fact that the one-component electron model used
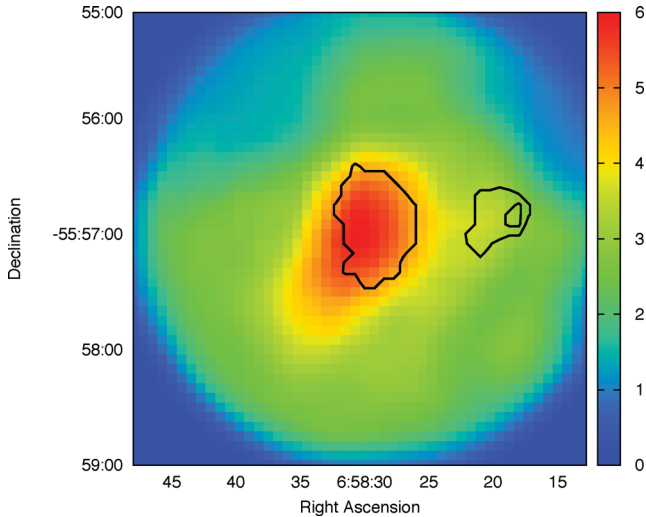
Figure 8. The modelled SZ intensity map at 600 GHz (same as in Fig. 3) and the integrated squared electron number density map, derived by assuming the model with two thermal components.

for the modelling of the SZ map cannot properly fit the X-ray data from *Chandra* because of the presence of a non-thermal-like component (Million & Allen 2009). We also plot the modelled SZ intensity and integrated squared electron number density maps, derived by assuming the model with two thermal components (the depth of a very hot component is 10 kpc), in Fig. 8. Since an offset between the SZ and integrated squared electron number density maxima is not present in Figs 6 and 8, we conclude that the inclusion of an additional hotter thermal component into the initial one-component thermal model provides us with an approach to reconcile the results of numerical simulations with that of the high-resolution X-ray and SZ observations.

5 CONCLUSIONS

Observations of X-ray emission from galaxy clusters with the *Chandra*, *XMM* and *Suzaku* satellites at energies lower than 10 keV have significantly improved our knowledge of the morphology and thermal structure of hot intracluster plasma. The X-ray observations of the Bullet cluster by *Chandra* with the longest exposure of 530 ks demonstrate evidence of non-thermal-like emission from this galaxy cluster (Million & Allen 2009). The hard X-ray emission excess from the Bullet cluster at energies higher than 15 keV that was found by Petrosian et al. (2006) and Ajello et al. (2010) with the *RXTE* and *Swift* satellites, respectively, also suggests the existence of either a very hot thermal or a non-thermal power-law electron component. However, it is difficult to distinguish between additional very hot thermal and non-thermal power-law X-ray components using only soft and hard X-ray observations.

We performed an analysis of the *Chandra* data for the Bullet cluster assuming the presence of additional very hot thermal and non-thermal power-law electron components and found the best-fitting values of the MEKAL parameter and temperature for all the thermal components. Using the relativistically correct Wright formalism, we calculated the SZ intensity maps and found that the morphology of the SZ intensity maps is different in the different models of the X-ray non-thermal-like emission. This allows us to test different interpretations of the X-ray emission excess from the Bullet cluster using X-ray and SZ instruments with high angular resolutions, such as *Chandra*-ACIS and *Herschel*-SPIRE. Compar-

ing the observed and modelled SZ intensity map morphologies, we conclude that the model including a very hot thermal component with the depth of several tenths of kpc is more consistent with the *Herschel* SZ observations of the Bullet cluster at a frequency of 600 GHz.

We use the numerical simulations performed by Akahori & Yoshikawa (2012) to calculate an SZ intensity map of the Bullet cluster and to compare the simulated SZ intensity map with those derived in the one-component model and in the model with two thermal components (the depth of a very hot component is 10 kpc). Comparing the simulated SZ intensity map with that modelled from X-ray observations, we found that the offset between the SZ and integrated squared electron number density for the eastern substructure is only present on the SZ intensity map derived by assuming the one-component thermal model. This difference can be explained by the fact that the one-component electron model used for modelling of the SZ intensity map cannot properly fit the X-ray data.

We conclude that the SZ and X-ray morphologies can be different from each other because of the presence of additional high-energy electron populations which cause the observed X-ray emission excess in the Bullet cluster. The present high-resolution SZ instruments, such as SPIRE on the *Herschel* satellite, MUSTANG on the Green Bank Telescope and LABOCA at the Atacama Pathfinder Experiment (APEX), have sufficient angular resolution and sensitivity to test for the presence of various additional high-energy electron populations in galaxy clusters with X-ray emission excesses.

REFERENCES

Ajello M., Rebusco P., Cappelluti N., Reimer O., Böhringer H., La Parola V., Cusumano G., 2010, ApJ, 725, 1688
Akahori T., Yoshikawa K., 2010, PASJ, 62, 335
Akahori T., Yoshikawa K., 2012, PASJ, 64, 12
Arnaud K. A., 1996, in Jacoby G., Barnes J., eds, ASP Conf. Ser. Vol. 101. Astronomical Data Analysis Software and Systems V. Astron. Soc. Pac., San Francisco, p. 17
Balucinska-Church M., McCammon D., 1992, ApJ, 400, 699
Birkinshaw M., 1999, Phys. Rep., 310, 97
Brunetti G., Lazarian A., 2007, MNRAS, 378, 245
Challinor A., Lasenby A., 1998, ApJ, 499, 1
Colafrancesco S., Marchegiani P., Buonanno R., 2011, A&A, 527, L1
Dogiel V. A., Colafrancesco S., Ko C. M., Kuo P. H., Hwang C. Y., Ip W. H., Birkinshaw M., Prokhorov D. A., 2007, A&A, 461, 433
Enßlin T. A., Kaiser C. R., 2000, A&A, 360, 417
Ferrari C., Govoni F., Schindler S., Bykov A. M., Rephaeli Y., 2008, Space Sci. Rev., 134, 93
Itoh N., Nozawa S., 2004, A&A, 417, 827
Itoh N., Kohyama Y., Nozawa S., 1998, ApJ, 502, 7
Kaastra J. S., Mewe R., 1993, Legacy, 3, 16
Kalberla P. M. W., Burton W. B., Hartmann D., Arnal E. M., Bajaja E., Morras R., Poppel W. G. L., 2005, A&A, 440, 775
Korngut P. M. et al., 2011, ApJ, 734, 10

Liang H., Hunstead R. W., Birkinshaw M., Andreani P., 2000, ApJ, 544, 686
Malu S. S., Subrahmanyan R., Wieringa M., Narasimha D., 2010, preprint (arXiv:1005.1394)
Markevitch M., 2006, in Wilson A., ed., ESA Special Publ. Vol. 604, The X-ray Universe 2005. ESA, Noordwijk, p. 723
Markevitch M., Gonzalez A. H., David L., Vikhlinin A., Murray S., Forman W., Jones C., Tucker W., 2002, ApJ, 567, L27
Mason B. S. et al., 2010, ApJ, 716, 739
Mastropietro C., Burkert A., 2008, MNRAS, 389, 967
Million E. T., Allen S. W., 2009, MNRAS, 399, 1307
Narravo J. F., Frenk C. S., White S. D. M., 1997, ApJ, 490, 493
Nord M. et al., 2009, A&A, 506, 623
Nozawa S., Kohyama Y., 2009, Phys. Rev. D, 79, 083005
Nozawa S., Itoh N., Kawana Y., Kohyama Y., 2000, ApJ, 536, 31
Petrosian V., Madejski G., Luli K., 2006, ApJ, 652, 948
Prokhorov D. A., Colafrancesco S., 2012, MNRAS, 424, L49

Prokhorov D. A., Antonuccio-Delogu V., Silk J., 2010, A&A, 520, A106
Prokhorov D. A., Dubois Y., Nagataki S., Akahori T., Yoshikawa K., 2011a, MNRAS, 415, 2505
Prokhorov D. A., Colafrancesco S., Akahori T., Million E. T., Nagataki S., Yoshikawa K., 2011b, MNRAS, 416, 302
Rephaeli Y., 1979, ApJ, 227, 364
Rephaeli Y., 1995, ApJ, 445, 33
Sanders J. S., 2006, MNRAS, 371, 829
Springel V., Farrar G., 2007, MNRAS, 380, 911
Timokhin A. N., Aharonian F. A., Neronov A. Y., 2004, A&A, 417, 391
Wright E. L., 1979, ApJ, 232, 348
Yamada K. et al., 2012, preprint (arXiV:1203.5929)
Zemcov M. et al., 2010, A&A, 518, L16

This paper has been typeset from a TEX/LATEX file prepared by the author.